



Cite this: *J. Mater. Chem. A*, 2023, 11, 8173

# Unveiling a high capacity multi-redox (Nb<sup>5+</sup>/Nb<sup>4+</sup>/Nb<sup>3+</sup>) NASICON-Nb<sub>2</sub>(PO<sub>4</sub>)<sub>3</sub> anode for Li- and Na-ion batteries†

Bi-lab Patra,<sup>a</sup> Keshav Kumar,<sup>a</sup> Debolina Deb,<sup>b</sup> Subham Ghosh,<sup>a</sup> Gopalakrishnan Sai Gautam<sup>b</sup> and Premkumar Senguttuvan<sup>a\*</sup>

Sodium superionic conductor (NASICON)-type materials are widely explored as Li- and Na-ion cathodes and solid-state electrolytes but are largely ignored as anodes due to their lower capacities and higher intercalation voltages, which reduce the overall energy densities of Li- and Na-ion batteries (LIBs and SIBs). Herein, we unveil high capacity multi-redox empty NASICON-Nb<sub>2</sub>(PO<sub>4</sub>)<sub>3</sub> as a potential anode material for LIBs and SIBs, which reversibly delivers 167 and 150 mA h g<sup>-1</sup> at the average voltages of 1.86 V vs. Li<sup>+</sup>/Li<sup>0</sup> and 1.46 V vs. Na<sup>+</sup>/Na<sup>0</sup>, respectively. The Li and Na intercalation reactions proceed via multiple phase transitions, leading to short-range ordered Li<sub>3</sub>Nb<sub>2</sub>(PO<sub>4</sub>)<sub>3</sub> and triclinic (*P* $\bar{1}$ ) Na<sub>3</sub>Nb<sub>2</sub>(PO<sub>4</sub>)<sub>3</sub>, as revealed by *in situ* X-ray diffraction studies. Our density functional theory calculations are also in agreement with the *in situ* measurements in predicting a stable Na<sub>3</sub>Nb<sub>2</sub>(PO<sub>4</sub>)<sub>3</sub> composition in the Na-Nb<sub>2</sub>(PO<sub>4</sub>)<sub>3</sub> pseudo-binary system. X-ray absorption spectroscopy confirms the participation of multi-redox Nb<sup>5+</sup>/Nb<sup>4+</sup>/Nb<sup>3+</sup> couples. The Nb<sub>2</sub>(PO<sub>4</sub>)<sub>3</sub> anode delivers capacities greater than 124 and 106 mA h g<sup>-1</sup> at 1C rate in Li and Na cells, respectively. Pairing Nb<sub>2</sub>(PO<sub>4</sub>)<sub>3</sub> with suitable cathodes and electrolytes can lead to high energy density batteries.

Received 28th July 2022  
Accepted 9th February 2023

DOI: 10.1039/d2ta05971a

rsc.li/materials-a



*Dr. Premkumar Senguttuvan is currently an Associate Professor at New Chemistry Unit and International Centre for Materials Science, Jawaharlal Nehru Centre for Advanced Scientific Research, India. He received his MS degree from Université de Picardie Jules Verne – France (2010). He pursued his PhD under the guidance of Prof. J. M. Tarascon and Prof. M. R. Palacin at UPJV-France and ICMAB-*

*Spain (2010–2013). Thereafter, he worked as a Postdoctoral Associate in Dr C. S. Johnson's group at Argonne National Laboratory, USA (2014–2016). His research interests are solid-state chemistry, electrochemistry and rechargeable batteries. His recent honors include the DAE-BRNS Young Scientist's Research Award (2019) and DST-Early Career Research Award (2017).*

<sup>a</sup>New Chemistry Unit, International Centre for Materials Science and School of Advanced Materials, Jawaharlal Nehru Centre for Advanced Scientific Research, Jakkur, Bengaluru-560064, India. E-mail: prem@jncasr.ac.in

<sup>b</sup>Department of Materials Engineering, Indian Institute of Science, Bengaluru-560012, India

## Introduction

The demand for low-cost and sustainable battery technologies is continuously increasing to achieve carbon neutrality.<sup>1,2</sup> At present, Li-ion batteries are used extensively in portable electronics and electric vehicles, and their Na-ion analogues have emerged as the front-runner for grid storage applications.<sup>3–5</sup> Nevertheless, there exist many technical challenges for improving the performance of such batteries, in terms of higher energy and power densities, enhanced safety, and long-term cyclability.<sup>6,7</sup> Since these performance metrics are deeply connected with the materials used, the need for advanced Li- and Na-ion electrodes and electrolytes is continuously growing.<sup>8</sup>

While graphite and hard carbon are widely used in commercial Li-ion and prototypical Na-ion cells, respectively, they pose a serious risk of lithium and sodium metal plating at higher current densities, besides their lower volumetric energy densities.<sup>9</sup> Alternatively, intercalation-type transition metal oxides insert lithium and sodium ions at relatively higher voltages (>1.0 V), which may avoid electrolyte decomposition, and Li and Na metal electrodeposition.<sup>10</sup> In the case of LIBs, the

† Electronic supplementary information (ESI) available. See DOI: <https://doi.org/10.1039/d2ta05971a>

$\text{Li}_4\text{Ti}_5\text{O}_{12}$  anode reversibly exchanges Li ions at 1.5 V vs.  $\text{Li}^+/\text{Li}^0$  with a capacity of  $\sim 175 \text{ mA h g}^{-1}$ .<sup>11</sup> Recently, Wadsley–Roth crystallographic shear phases such as  $\text{TiNb}_2\text{O}_7$ ,<sup>12,13</sup>  $\text{VNb}_9\text{O}_{25}$ ,<sup>14</sup> and  $\text{Ti}_2\text{Nb}_{10}\text{O}_{29}$  have attracted much interest as Li-ion anodes due to their higher capacities ( $200\text{--}380 \text{ mA h g}^{-1}$ )<sup>15</sup> and excellent rate performances ( $\text{TiNb}_2\text{O}_7$  delivers capacities of 236, 219, 195 and  $128 \text{ mA h g}^{-1}$  at 5, 10, 20 and 50C rates, respectively). Similarly, few transition metal oxides such as  $\text{Na}_2\text{Ti}_3\text{O}_7$ ,<sup>16</sup>  $\text{TiO}_2$ ,<sup>17</sup> and  $\text{Li}_4\text{Ti}_5\text{O}_{12}$  have<sup>18</sup> been investigated as potential Na-ion hosts with moderate capacities ( $100\text{--}170 \text{ mA h g}^{-1}$ ) and limited cycle life.

Apart from oxides, transition metal-based polyanionic compounds such as sodium superionic conductor (NASICON) frameworks have been explored as possible Li- and Na-ion anodes. NASICON frameworks are appealing as electrodes<sup>19–23</sup> and solid-electrolytes<sup>24,25</sup> for Li- and Na-ion battery applications owing to their higher chemical, structural and thermal stabilities, and higher Na-ion conductivity. Their general chemical composition can be given as  $\text{A}_a\text{M}_2(\text{XO}_4)_3$  ( $\text{A} = \text{Li}$  and  $\text{Na}$ ;  $\text{M} = \text{Sc}$  to  $\text{Fe}$ ,  $\text{Zr}$  to  $\text{Mo}$ ,  $\text{In}$  and  $\text{Sn}$ ;  $\text{X} = \text{Si}$ ,  $\text{P}$ ,  $\text{S}$ ;  $0 \leq a \leq 4$ ) and structures are built from lantern units consisting of two  $\text{MO}_6$  octahedra and three  $\text{XO}_4$  tetrahedra, stacked along the  $c$ -axis.<sup>26,27</sup> Due to their size differences, Li and Na ions occupy different crystallographic sites in the NASICON framework (Li ions into the  $18f$  site of the  $R\bar{3}$  & Na ions into  $6b/18e$  sites of the  $R\bar{3}c$ ).<sup>28,29</sup> In principle, NASICON compounds can reversibly exchange a maximum of four moles of Li and Na ions, if provided with suitable redox centers.

Experimentally,  $\text{ATi}_2(\text{PO}_4)_3$  ( $\text{A} = \text{Li}$  and  $\text{Na}$ ) NASICONs reversibly (de)intercalate two moles of Li- and Na-ions at 2.6 and 2.1 V vs.  $\text{Li}^+/\text{Li}^0$  and  $\text{Na}^+/\text{Na}^0$ , respectively, through the redox activity of the  $\text{Ti}^{4+}/\text{Ti}^{3+}$  couple.<sup>30–32</sup> Upon reducing the lower cut-off voltage beyond  $\text{Na}_3\text{Ti}_2(\text{PO}_4)_3$ , an additional mole of sodium can be intercalated at 0.45 V with concomitant reduction of  $\text{Ti}^{3+}/\text{Ti}^{2+}$ , accounting for a total capacity of  $150 \text{ mA h g}^{-1}$ .<sup>33</sup> Another NASICON- $\text{Na}_3\text{V}_2(\text{PO}_4)_3$  reversibly exchanges Na ions at a lower voltage ( $\sim 1.6 \text{ V vs. Na}$ ) but shows a limited capacity of  $60 \text{ mA h g}^{-1}$  (i.e., equivalent to intercalation of one mole of sodium ions).<sup>34,35</sup> Also, a mixed NASICON compound,  $\text{TiNb}(\text{PO}_4)_3$ , has been preliminarily explored for Na intercalation ( $\sim 120 \text{ mA h g}^{-1}$ ).<sup>36</sup> Thus, NASICON cathodes and anodes explored so far operate within the limit of three moles of lithium- and/or sodium-ion exchange during cycling, thus leading to maximum storage capacities of  $140\text{--}160 \text{ mA h g}^{-1}$ .<sup>37–39</sup> Moreover, in terms of synthesis, NASICONs usually contain Na (or Li) ions as synthesized (e.g.,  $\text{Na}_3\text{V}_2(\text{PO}_4)_3$  is a NASICON composition that can be synthesized)<sup>40</sup> and electrochemical/chemical oxidation routes have to be employed to remove Na (or Li).<sup>41</sup>

In this work, we report for the first time the synthesis of polycrystalline “empty” NASICON- $\text{Nb}_2(\text{PO}_4)_3$  and its potential application as an anode in LIBs and SIBs. Previously Leclaire *et al.* reported its crystal structure using a single crystal of  $\text{Nb}_2(\text{PO}_4)_3$ .<sup>42</sup> This compound contains no Li or Na ions in its pristine state and is expected to exchange higher amount ( $\sim 3$  moles per formula unit) of lithium and sodium ions through the activity of multi-redox- $\text{Nb}^{5+}/\text{Nb}^{4+}/\text{Nb}^{3+}$  centers at relatively lower voltages than the Ti- or V-based NASICON anodes. In

addition to our electrochemical and characterization measurements, we have also performed first-principles calculations to understand the Na-intercalation phase behavior better. We believe that pairing this “empty” NASICON anode with suitable Na-ion cathodes and/or solid electrolytes (which can also be NASICON-based) can enable building high energy density Na-ion batteries.

## Experimental

### Synthesis

Empty NASICON- $\text{Nb}_2(\text{PO}_4)_3$  was prepared by high-temperature solid-state synthesis.  $\text{Nb}_2\text{O}_5$  (0.9 mmol) (Sigma Aldrich, 99.5%),  $\text{P}_2\text{O}_5$  (1.5 mmol) (Alfa Aesar, 99.0%), and Nb-powder (0.2 mmol) (Alfa Aesar, 99.8%) were mixed using a high-energy ball miller (SPEX 8000M) for 20 min. The resulting mixture was then placed in an evacuated quartz ampoule and sealed under high vacuum of  $10^{-6}$  mbar. The tube was slowly heated up to 1473 K in 35 hours followed by dwelling at this temperature for 72 hours and then cooled back to room temperature in 7 hours. Finally, the tube was opened in an Ar-filled glove box and the final powder product was collected.

### Characterization

Synchrotron powder diffraction patterns were collected on  $\text{Nb}_2(\text{PO}_4)_3$  and  $\text{Na}_3\text{Nb}_2(\text{PO}_4)_3$  sealed in a Kapton capillary (0.5 mm diameter) at the 11-BM beamline ( $\lambda = 0.458969 \text{ \AA}$ ) of the Advanced Photon Source, Argonne National Laboratory, and the data were analyzed using the FullProf program.<sup>43</sup> FESEM images were taken using a Zeiss Gemini SEM 500 to observe the morphology and homogeneous distribution of the elements.

Electrochemical testing of  $\text{Nb}_2(\text{PO}_4)_3$  was carried out in two-electrode Swagelok cells using either lithium or sodium (99.9% Aldrich) metal as the counter electrode in galvanostatic mode.  $\text{Nb}_2(\text{PO}_4)_3$  electrodes were prepared by ball milling as-synthesized samples with Super C45 (Timcal) in a 70 : 30 ratio for 8 min. The ball-milled mixture was collected and mixed with polyvinylidene fluoride (PVDF) (in such a way that the final electrode contains active material : carbon : PVDF in a weight ratio of 65 : 27 : 8) in *N*-methyl-2-pyrrolidone (NMP) solvent. The resulting slurry was uniformly coated on Cu foil, followed by drying in a vacuum oven at 90 °C for 6 hours. The dried electrodes were punched into round discs of 10 mm diameter. The active material loading of the final electrode was estimated to be  $2.5\text{--}3.0 \text{ mg cm}^{-2}$ . Sodium cells were assembled using a 1 M solution of  $\text{NaPF}_6$  (Sigma, 98%) in diglyme (Sigma, 99.5%) as an electrolyte with sodium metal as the counter electrode. Similarly, lithium cells were fabricated using a 1 M electrolyte solution of  $\text{LiPF}_6$  in EC:DMC and lithium metal as the counter electrode. The cells were assembled in an Ar-filled glove box ( $\text{O}_2 < 0.1 \text{ ppm}$  and  $\text{H}_2\text{O} < 0.1 \text{ ppm}$ ) and tested in a battery cycler (BT-lab, Biologic) using the galvanostatic protocol. For galvanostatic intermittent titration technique (GITT) experiments, first, the cells were cycled at C/10 for three cycles then a current equivalent to a C/10 rate was applied for 1 h followed by a 4 h relaxation.

For *in situ* XRD measurements, the  $\text{Nb}_2(\text{PO}_4)_3$  anode was coated on pinhole-free thin aluminum foil (Alfa, 99.99%, 10 mm thickness) and a home-made *in situ* cell fitted with a Be-window was used for the experiment. XRD patterns at different states-of-charge were collected using the same Bruker D8-diffractometer and Le-Bail fitting was performed using the Fullprof program.

X-ray absorption spectroscopy (XAS) measurements of pristine and cycled electrodes at different states-of-charge were carried out at PETRA-III beamline P65 at DESY in Hamburg. The measurements of the Nb–K edge at room temperature were performed in fluorescence mode as well as transmission mode using gas ionization chambers to monitor the intensities of the incident and transmitted X-ray using a PIPS diode. The energy of the Nb–K edge was calibrated by defining the inflection point (first derivative maxima) of Nb foil as 18 987.5 eV.  $\text{Nb}_2\text{O}_5$  and  $\text{NbO}_2$  were used as standard materials. The standard materials were thoroughly mixed with boron nitride and pressed into 12 mm pellets of 1 mm thickness and *ex situ* electrodes were sealed in between Kapton tapes inside an Ar-filled glove box and used directly for the data collection. All data were collected at room temperature with a Si (111) double crystal monochromator and all XAS spectra were processed using the DEMETER software package.<sup>44,45</sup>

## Computations

Density functional theory (DFT) calculations were performed using the Vienna *ab initio* simulation package (VASP),<sup>46,47</sup> which employs a plane wave basis (energy cut-off of 520 eV) and projector augmented wave<sup>48</sup> potentials. To describe the electronic exchange and correlation, we used the strongly constrained and appropriately normed<sup>49</sup> functional. We used a  $\Gamma$ -centred  $k$ -point mesh to sample the Brillouin zone with a density of at least 32  $k$ -points per Å. We relaxed the lattice vectors, cell shape, and cell volume of all structures, without preserving the underlying symmetry, with structures considered converged when the total energies and atomic forces drop below 0.01 meV and  $|0.03| \text{ eV \AA}^{-1}$ . We obtained the initial structure of  $\text{Nb}_2(\text{PO}_4)_3$  from the inorganic crystal structure database<sup>50</sup> and we took the equivalent Na positions from the  $\text{Na}_4\text{V}_2(\text{PO}_4)_3$  cathode NASICON structure. The Na-vacancy orderings at  $\text{NaNb}_2(\text{PO}_4)_3$ ,  $\text{Na}_2\text{Nb}_2(\text{PO}_4)_3$ , and  $\text{Na}_3\text{Nb}_2(\text{PO}_4)_3$  compositions were enumerated using the pymatgen<sup>51</sup> package within the primitive cell (containing two  $\text{Nb}_2(\text{PO}_4)_3$  formula units) and a  $2 \times 1 \times 1$  supercell of the primitive NASICON structure. The procedure to calculate average voltages, which neglect  $pV$  and entropic contributions, is detailed in our previous studies.<sup>52,53</sup>

## Results and discussion

Polycrystalline  $\text{NASICON-Nb}_2(\text{PO}_4)_3$  was prepared through a classical solid-state synthesis route using  $\text{Nb}_2\text{O}_5$ , Nb, and  $\text{P}_2\text{O}_5$  precursors (for details, see the Experimental section). Fig. 1a shows the Rietveld refinement of the synchrotron X-ray diffraction (XRD) pattern collected on  $\text{NASICON-Nb}_2(\text{PO}_4)_3$  at room temperature. The XRD pattern can be completely indexed

with  $R\bar{3}c$  space group, thus confirming the phase purity of the sample. The scanning electron microscopy (SEM) image of  $\text{NASICON-Nb}_2(\text{PO}_4)_3$  (inset of Fig. 1a) shows the presence of irregular micron-sized ( $\sim 10 \mu\text{m}$ ) primary particles and elemental mapping shows the homogeneous distribution of Nb, P, and O in the sample (Fig. S1†). The calculated lattice parameters ( $a = 8.6629(1)$  and  $c = 22.0627(6)$  Å) and atomic coordinates of the  $\text{NASICON-Nb}_2(\text{PO}_4)_3$  structure are displayed in Table S1 in the ESI.† Its crystal structure is built from lantern units,<sup>42</sup> consisting of two  $(\text{Nb}^{5+}/\text{Nb}^{4+})\text{O}_6$  and three  $\text{PO}_4$  units, stacked along the  $c$ -direction (Fig. 1b) and both Na(1) and Na(2) (*i.e.*, 6b and 18e, respectively) sites are empty. To probe the oxidation state of Nb in  $\text{NASICON-Nb}_2(\text{PO}_4)_3$ , X-ray absorption spectroscopy measurements were performed along with  $\text{Nb}_2\text{O}_5$  and  $\text{NbO}_2$  references. Their corresponding normalized X-ray absorption near-edge structure (XANES) spectra collected at the Nb K-edge are shown in Fig. 1c. The absorption edge position of  $\text{Nb}_2(\text{PO}_4)_3$  is found to be between those of  $\text{Nb}_2\text{O}_5$  and  $\text{NbO}_2$ , thus confirming the presence of both  $\text{Nb}^{5+}$  and  $\text{Nb}^{4+}$  in the NASICON lattice.

The  $\text{NASICON-Nb}_2(\text{PO}_4)_3$  anode is expected to reversibly exchange three moles of Li- and Na-ions through redox activities of  $\text{Nb}^{5+}/\text{Nb}^{4+}$  and  $\text{Nb}^{4+}/\text{Nb}^{3+}$  centers, leading to a theoretical capacity of  $\sim 171 \text{ mA h g}^{-1}$ . First, we studied the electrochemical Li-ion (de)intercalation property of the  $\text{NASICON-Nb}_2(\text{PO}_4)_3$  anode in Li half cells. The voltage-capacity plot of the  $\text{Nb}_2(\text{PO}_4)_3/\text{Li}$  cell cycled at C/10 rate in a voltage window of 3.0–1.2 V vs.  $\text{Li}^+/\text{Li}^0$  is displayed in Fig. 2a. During the first discharge, this cell exhibits two voltage plateaus at  $\sim 2.3$  and 1.6 V vs.  $\text{Li}^+/\text{Li}^0$  followed by a sloping curve until 1.2 V vs.  $\text{Li}^+/\text{Li}^0$  with a total discharge capacity of  $257 \text{ mA h g}^{-1}$ . On the subsequent charge, the two-step voltage profile is reversed with a charge capacity of  $167 \text{ mA h g}^{-1}$ , which is equivalent to the deintercalation of  $\sim 2.9$  moles of Li-ions from the  $\text{Nb}_2(\text{PO}_4)_3$  framework. Nearly 1.5 moles of lithium-ions are lost during the first cycle, which could be due to electrolyte decomposition. The voltage-capacity profiles from the subsequent cycles overlap with each other with capacities of  $\sim 167 \text{ mA h g}^{-1}$ . The corresponding  $dQ/dV$  curves (Fig. 2b) show two oxidation/reduction peaks located at 2.31/2.29 and 1.65/1.55 V vs.  $\text{Li}^+/\text{Li}^0$ , which could be tentatively assigned to the operation of  $\text{Nb}^{5+}/\text{Nb}^{4+}$  and  $\text{Nb}^{4+}/\text{Nb}^{3+}$  redox couples, respectively.

To better understand the structural evolution of the  $\text{NASICON-Nb}_2(\text{PO}_4)_3$  anode upon Li (de)intercalation, we performed an *in situ* XRD measurement at C/15 rate during the first cycle (Fig. 2c and d) and the evolution of corresponding lattice parameters is displayed in Fig. 2e. Initially, a small solid-solution region is noticed for a  $\Delta x = 0.2$  moles of Li-ion intercalation into the  $\text{NASICON-Nb}_2(\text{PO}_4)_3$  anode with subtle changes in the lattice parameters ( $\Phi_A$ :  $\text{Li}_{0-0.2}\text{Nb}_2(\text{PO}_4)_3$ ). As the discharge proceeds through the voltage plateau at  $\sim 2.25$  V vs.  $\text{Li}^+/\text{Li}^0$ , we find a new set of reflections along with the parent  $\text{NASICON-Nb}_2(\text{PO}_4)_3$ , indicating a two-phase intercalation mechanism ( $\Phi_B$ :  $\text{Li}_{1.3-3.0}\text{Nb}_2(\text{PO}_4)_3$ ). However, the peak positions of both NASICON phases slightly drift as Li-ion intercalation proceeds, similar to  $\text{LiVOPO}_4$  and  $\text{Na}_3\text{V}_2(\text{PO}_4)_2\text{F}_3$  cathodes.<sup>54,55</sup> The XRD pattern collected at the end of 1.5 V shows anisotropic lattice parameter

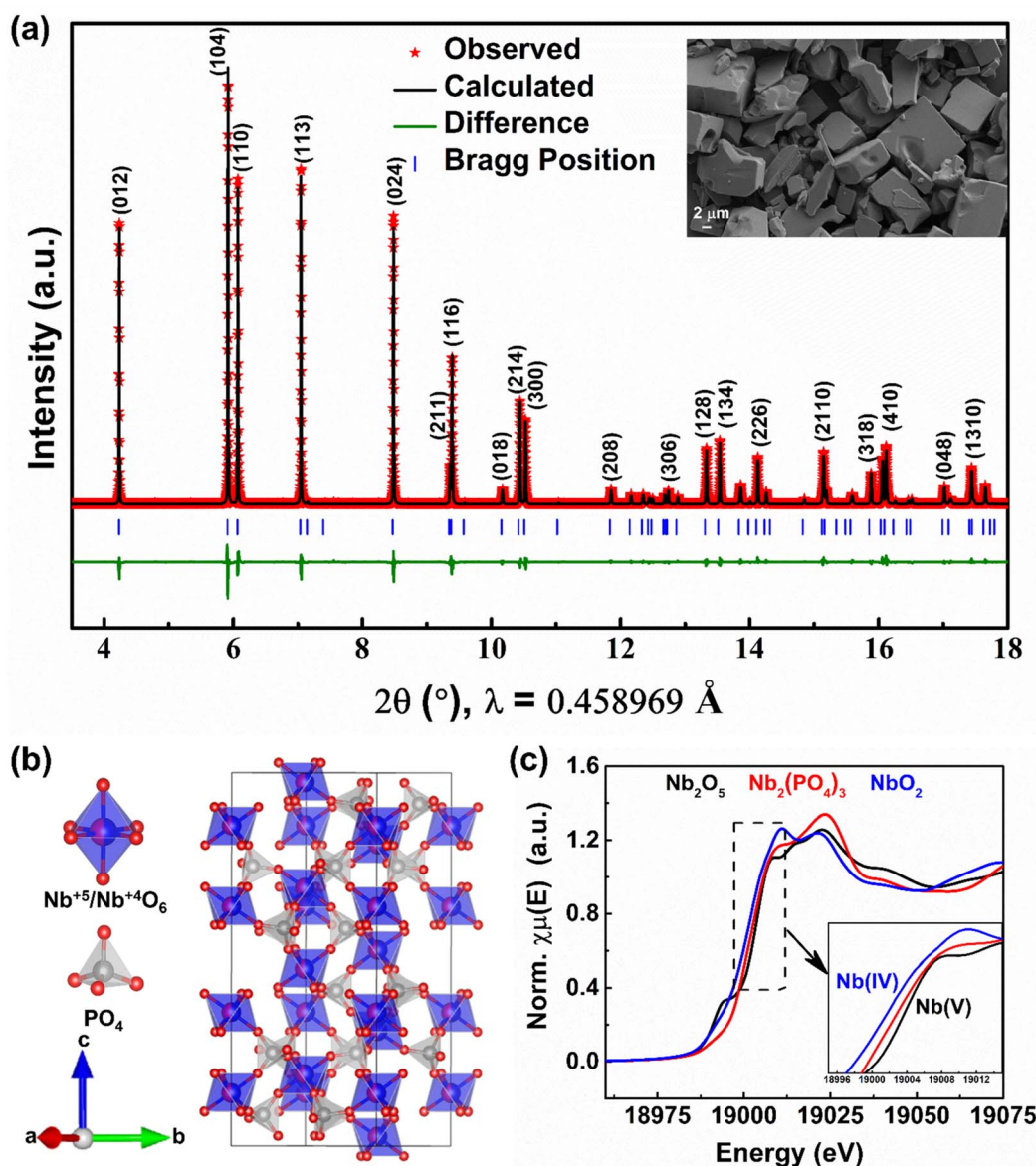


Fig. 1 (a) Rietveld refinement of the room temperature synchrotron XRD pattern (inset: SEM image), (b) crystal structure, and (c) XANES spectra collected at the Nb K-edge of NASICON- $\text{Nb}_2(\text{PO}_4)_3$ .

changes, *i.e.*,  $\Delta a/a = +1.21\%$  and  $\Delta c/c = -3.06\%$ , with a nominal overall unit cell volume reduction of  $\Delta v/v = -0.69\%$ . Further, as the voltage descends to 1.2 V *vs.*  $\text{Li}^+/\text{Li}^0$ , we notice a smoother variation of peak positions, signifying solid-solution behavior. It is worth mentioning that the XRD patterns collected closer to 1.2 V present weaker reflections, implying the formation of short-range ordered “ $\text{Li}_3\text{Nb}_2(\text{PO}_4)_3$ ” at the end of discharge. Note that the extra capacity (*i.e.*, 4 moles of  $\text{Li}^+$  insertion) observed during the first discharge can be accounted for electrolyte decomposition as mentioned earlier. The overall volume change between the fully lithiated and pristine NASICON phases is estimated as  $\Delta v/v = +0.03\%$ . Interestingly, upon subsequent charging the above-mentioned phenomena are reversed sequentially and the XRD pattern collected at the end of 1st cycle nearly superimposes on that of the pristine electrode, indicating excellent reversibility

of the Li-ion (de)intercalation reaction. Further, the *in situ* XRD patterns collected during the second cycle quite resemble the first cycle patterns, thus confirming the same Li-ion (de)intercalation pathway in the successive cycles (Fig. S2<sup>†</sup>). It is worth mentioning that the limited quality of XRD patterns impedes us from solving the crystal structures of Li-rich NASICON phases obtained during discharge, especially given the large configurational space for Li to arrange itself in the NASICON lattice. Thus, advanced local and bulk structural studies along with DFT calculations are required to elucidate the Li-ion (de)intercalation mechanism of the  $\text{Nb}_2(\text{PO}_4)_3$  anode.

The voltage–capacity profiles of  $\text{Nb}_2(\text{PO}_4)_3/\text{Na}$  cell cycled at C/10 rate in a voltage window of 3.0–1.05 V *vs.*  $\text{Na}^+/\text{Na}^0$  are displayed in Fig. 3a. In contrast to its Li counterpart, the  $\text{Nb}_2(\text{PO}_4)_3/\text{Na}$  cell exhibits a shorter voltage step at  $\sim 2.35$  V *vs.*

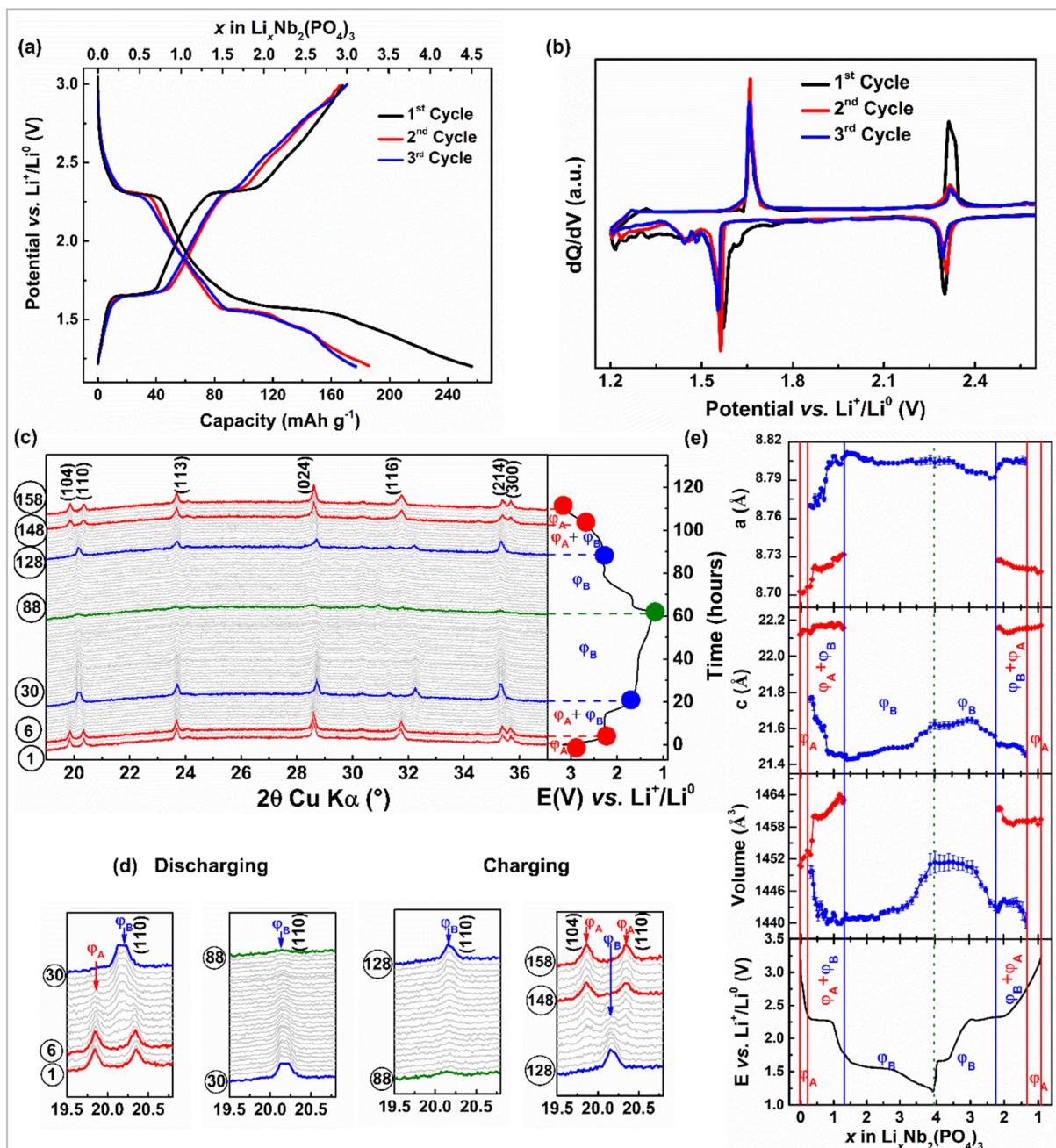


Fig. 2 (a) Voltage vs. capacity and (b)  $dQ/dV$  profiles of the  $\text{Nb}_2(\text{PO}_4)_3/\text{Li}$  cell. (c and d) *in situ* XRD patterns of the  $\text{Nb}_2(\text{PO}_4)_3$  anode and (e) its cell parameter evolution during the first cycle of Li-ion (de)intercalation (vertical solid and dotted lines indicate the phase boundaries during Li-ion (de)intercalation).

$\text{Na}^+/\text{Na}^0$  (for  $\Delta x = 0.2 \text{ Na}^+$ ), which is followed by a sloping voltage curve until 1.2 V vs.  $\text{Na}^+/\text{Na}^0$  (for  $\Delta x = 2 \text{ Na}^+$ ) and a voltage plateau at  $\sim 1.14$  V vs.  $\text{Na}^+/\text{Na}^0$  with a total discharge capacity of  $226 \text{ mA h g}^{-1}$ . During the subsequent charge, these voltage features are partially reversible with a de-sodiation capacity of  $150 \text{ mA h g}^{-1}$  (*i.e.*, equivalent to 2.6 moles of Na-ion deintercalation from the  $\text{Nb}_2(\text{PO}_4)_3$  framework). A capacity of  $76 \text{ mA h g}^{-1}$  is lost during the first cycle, which could be due to electrolyte decomposition and/or partial entrapment of  $\text{Na}^+$  ions in the NASICON- $\text{Nb}_2(\text{PO}_4)_3$  framework.<sup>56,57</sup> The voltage–

capacity profiles of the second and third cycles neatly superimpose on each other with reversible capacities and coulombic efficiencies of  $\sim 150 \text{ mA h g}^{-1}$  and 95%, respectively. The corresponding  $dQ/dV$  profiles of the  $\text{Nb}_2(\text{PO}_4)_3/\text{Na}$  cell (Fig. 3b) show two oxidation/reduction peaks located at 2.4/2.3 and 1.22/1.12 V vs.  $\text{Na}^+/\text{Na}^0$  which could be attributed to the operation of  $\text{Nb}^{5+}/\text{Nb}^{4+}$  and  $\text{Nb}^{4+}/\text{Nb}^{3+}$  redox couples, respectively.

To follow the structural changes of the  $\text{Nb}_2(\text{PO}_4)_3$  anode upon Na-ion (de)intercalation, we carried out an *in situ* XRD measurement at C/15 rate during the first cycle (Fig. 3c and d). The

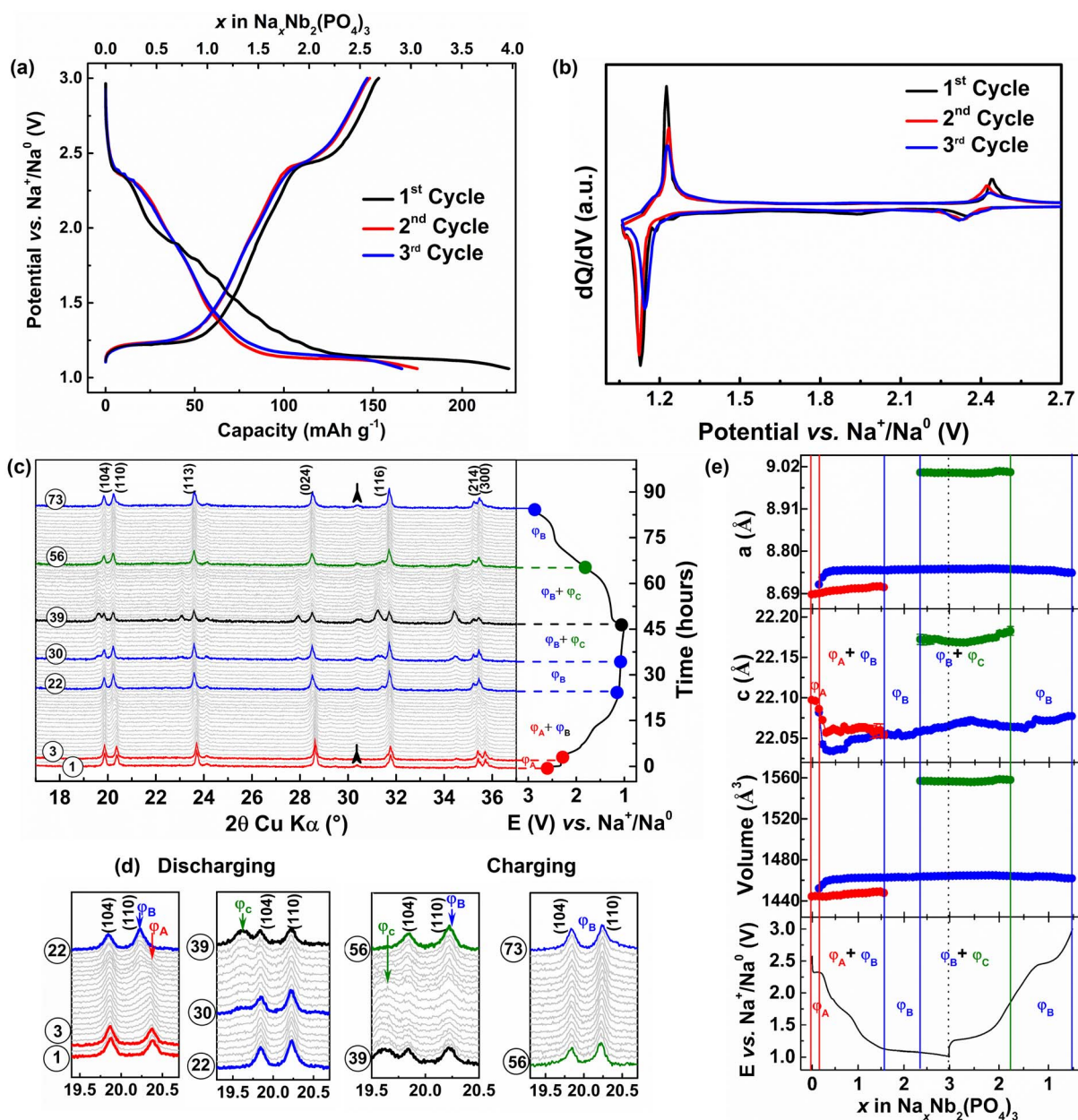


Fig. 3 (a) Voltage vs. capacity and (b)  $dQ/dV$  profiles of the  $\text{Nb}_2(\text{PO}_4)_3/\text{Na}$  cell. (c) and (d) *in situ* XRD patterns of the  $\text{Nb}_2(\text{PO}_4)_3$  anode and (e) its cell parameter evolution during the first cycle of  $\text{Na}$ -ion (de)intercalation (vertical solid and dotted lines indicate the phase boundaries during  $\text{Na}$ -ion (de)intercalation).

calculated lattice parameters of the XRD patterns are plotted against  $x$  in Fig. 3e. At the beginning of the first discharge (pattern #1–3), the formation of  $\text{Na}_{0.2}\text{Nb}_2(\text{PO}_4)_3$  (denoted as  $\Phi_A$  phase) from the parent  $\text{Nb}_2(\text{PO}_4)_3$  proceeds *via* a solid-solution mechanism, which is self-evident from moving of XRD peaks toward lower  $2\theta$  values. During this process, the changes in lattice parameters are less pronounced ( $\Delta a/a = +0.03\%$ ) and ( $\Delta c/c = -0.05\%$ ). The decrease of the  $c$ -parameter can be attributed to the filling of  $\text{Na}$ -ions into the  $\text{Na}(1)$  site, which diminishes the electrostatic repulsion between  $\text{NbO}_6$  octahedra. As the discharge proceeds to the next  $\Delta x = 1.4$  (pattern #4–22), a new set of reflections belonging to another NASICON phase ( $\Phi_B$ :  $\text{Na}_{1.6-2.3}\text{Nb}_2(\text{PO}_4)_3$ ) grows at the expense of the former  $\Phi_A$  phase (refer Fig. 3e), which is followed by

another narrow solid-solution region for  $\Delta x = 0.66$  (Pattern #23–30). The  $c$ -parameters of both NASICON ( $\Phi_A$  and  $\Phi_B$ ) phases initially decrease (due to the filling of the  $\text{Na}(1)$  site) and stabilize whereas their  $a$ -parameters do not change significantly. Beyond this point, the sodiation reaction associated with the low-voltage plateau (1.15 V vs.  $\text{Na}^+/\text{Na}^0$ ) continues *via* a two-phase mechanism, resulting in the formation of the third NASICON phase “ $\text{Na}_3\text{Nb}_2(\text{PO}_4)_3$ ” (denoted as  $\Phi_C$ ). During this process, the cell parameters and unit cell volume of  $\Phi_C$  increase ( $\Delta a/a = +3.64\%$ ,  $\Delta c/c = +0.32\%$ , and  $\Delta v/v = +7.77\%$ ) with the respect to the pristine NASICON phase. The increase of cell parameters can be correlated with the filling of sodium ions and the increase of  $\text{NbO}_6$  octahedra size (due to the reduction of  $\text{Nb}^{5+}/\text{Nb}^{4+}$  to  $\text{Nb}^{4+}/\text{Nb}^{3+}$ ).

Further, we collected the synchrotron powder XRD pattern of fully discharged  $\text{Na}_3\text{Nb}_2(\text{PO}_4)_3$  (cycled at C/50 rate) to elucidate its crystal structure (Fig. 4a and b). The XRD pattern can be completely indexed with  $(P\bar{1})$  space group with the cell parameters:  $a = 8.7153(2)$  Å,  $b = 9.0908(1)$  Å,  $c = 22.6495(1)$  Å,  $\alpha = 89.112(9)^\circ$ ,  $\beta = 90.052(9)^\circ$  and  $\gamma = 119.912(3)^\circ$ , similar to NASICON- $\text{Na}_3\text{Ti}_2(\text{PO}_4)_3$ .<sup>58,59</sup> In this structure, sodium ions fully and partially occupy Na(1a-d) and Na(2a-f) sites which correspond to the Na(1) and Na(2) sites of the  $R\bar{3}c$  structure, respectively. On the subsequent charge, the above-mentioned intercalation phenomena are mostly reversed, except the final XRD pattern (pattern #73) does not exactly match that of the pristine electrode. Indeed, its corresponding unit cell parameters and volume indicate the entrapment of Na-ions ( $\sim 0.6$  moles) in  $\text{Nb}_2(\text{PO}_4)_3$ , in agreement with our electrochemical results. Furthermore, the *in situ* XRD patterns collected during the second cycle display similar Na (de)intercalation phenomena as observed in the first cycle, confirming the reversibility of the (de)sodiation process (Fig. S3†).

To further understand the Na (de)intercalation phase behavior, we performed DFT calculations (see the Computations section), with the calculated 0 K formation energy and voltage values plotted as a function of Na concentration ( $x$ ) in  $\text{Nb}_2(\text{PO}_4)_3$  in Fig. 4c and d, respectively. The convex hull in Fig. 4c indicates that the stable ground states of  $\text{Na}_x\text{Nb}_2(\text{PO}_4)_3$  include the fully empty ( $\text{Nb}_2(\text{PO}_4)_3$ ), fully sodiated ( $\text{Na}_4\text{Nb}_2(\text{PO}_4)_3$ ), and partially sodiated ( $\text{Na}_3\text{Nb}_2(\text{PO}_4)_3$ ) configurations. Importantly, the ground state at  $x = 3$ , is similar to the ground state configurations observed in other NASICON cathode chemistries.<sup>52,53</sup> The  $\text{Na}_3\text{Nb}_2(\text{PO}_4)_3$  ground state has Na fully occupying the Na(1) site and partially occupying the Na(2) site, which is in line with our experimental observation as well (Fig. 4b). In contrast to other cathode chemistries, however, we don't observe a ground state configuration at  $x = 1$ ,<sup>52</sup> which explains the minor solubility ( $x \leq 0.2$ ) of Na in the empty  $\text{Nb}_2(\text{PO}_4)_3$  structure. In terms of average voltages (Fig. 4d), we predict a voltage plateau of  $\sim 1.06$  V between  $x = 0$  and 3, and  $\sim 0.93$  V between  $x = 3$  and 4, partly in agreement with our observed voltage plateau of  $\sim 1.15$  V vs. Na that represents a two-phase intercalation mechanism as well. Experimentally, we observe capacity degradation to occur whenever we attempt to cycle the  $\text{Na}_x\text{Nb}_2(\text{PO}_4)_3$  system below 1 V vs. Na. This capacity degradation can be due to electrolyte degradation and/or Na-entrapment. Note that computationally, we have calculated a two-phase voltage plateau to form at voltages below 1 V vs. Na, which will result in the formation of the  $\text{Na}_4\text{-Nb}_2(\text{PO}_4)_3$  phase. Previous computational studies on NASICON systems<sup>60</sup> showed that the Na conductivity (or diffusivity) drops significantly as Na content in NASICONs approach  $x_{\text{Na}} = 4$ . Moreover, the redox behavior may not be fully reversible from  $\text{Nb}^{2+}$  till  $\text{Nb}^{4+}$ , as reported with other transition metals as well within the NASICON framework.<sup>53</sup> Hence, we expect partial entrapment of Na to occur at voltage ranges below 1 V vs. Na, due to the formation of the  $\text{Na}_4\text{Nb}_2(\text{PO}_4)_3$  phase.

To monitor the changes in the Nb oxidation state and local structure, we performed X-ray absorption spectroscopy measurements. Fig. 4e displays the normalized XANES spectra of pristine, discharged, and charged electrodes collected at the Nb K-edge. As the discharge proceeds the XANES of the Nb K-edge shifts towards

lower energy values, indicating the reduction of  $\text{Nb}^{5+}/\text{Nb}^{4+}$  to  $\text{Nb}^{4+}/\text{Nb}^{3+}$ , and subsequently moves back to higher energy values at the end of the first charge. The corresponding Fourier-transformed extended X-ray absorption fine structure (EXAFS) plots are displayed in Fig. 4f. The peak located at 1.5 Å corresponds to the Nb–O shell, whereas the next three peaks located in between  $\sim 2.0$ – $3.25$  Å represent the second and third shells of Nb–P and Nb–Na pairs. The EXAFS data collected at the end of discharge shift towards higher Å values, indicating the expansion of the NASICON structure. Note that although the EXAFS data collected on the subsequent discharge shifts towards lower Å values, it doesn't match with that of the pristine electrode due to the entrapment of Na-ions in the NASICON framework. These observations are in agreement with our electrochemical and *in situ* XRD results. Furthermore, the fitting of EXAFS oscillations shows the increase of the average Nb–O bond length from 2.028 to 2.086 Å during discharge due to the reduction of niobium.

Our combined electrochemical and *in situ* experiments highlight the distinct intercalation behavior of the same NASICON- $\text{Nb}_2(\text{PO}_4)_3$  anode against Li and Na. For instance, the  $\text{Nb}_2(\text{PO}_4)_3/\text{Li}$  and  $\text{Nb}_2(\text{PO}_4)_3/\text{Na}$  cells exhibit flat and sloping voltage curves for the initial one mole of Li and Na ion intercalation, respectively, even though both mostly follow a two-phase mechanism. Moreover, the volume of the  $\text{Nb}_2(\text{PO}_4)_3$  unit cell shrinks along with the loss of long-range crystal order during the low voltage lithiation ( $\sim$ at 1.55 V vs.  $\text{Li}^+/\text{Li}^0$ ) whereas the same anode exhibits volume expansion upon the low voltage sodiation (at  $\sim 1.1$  V vs.  $\text{Na}^+/\text{Na}^0$ ). Hence, to better comprehend the Li and Na intercalation mechanism of the NASICON- $\text{Nb}_2(\text{PO}_4)_3$  anode, we performed galvanostatic intermittent titration technique (GITT) experiments during the fourth cycle (see the Experimental section for details, Fig. 5a and b).

Notably, both Li and Na GITT voltage vs. composition ( $x$  in  $\text{Li}_x\text{Nb}_2(\text{PO}_4)_3$  or  $\text{Na}_x\text{Nb}_2(\text{PO}_4)_3$ ) profiles present significant polarization between charge and discharge processes (even after 4 h relaxation). More importantly, the voltage jumps during the open circuit voltage (OCV) steps are prominent during charging compared to the discharging process, which is also reflected by the steep increase of internal resistance values and can be ascribed to slower solid-state Li and Na ion diffusion.<sup>61,62</sup> Such a difference could arise from various thermodynamic and kinetic factors involving structural and electrochemical properties of the NASICON host. As mentioned earlier, Li and Na ions prefer to occupy different crystallographic sites, which have distinct (electro)chemical potentials for (de)intercalation.<sup>63</sup> Moreover, it is well known that ionic conduction in the NASICON framework occurs *via* correlated ion migration through M(1)/M(2) pathways,<sup>24,64</sup> thus the relative filling of these sites can tune ionic conductivities and intercalation kinetics. Besides, the different chemical characters of Li and Na ions (*i.e.*, relative polarizability) can impart a different degree of interactions with the host lattice (such as distortion of polyhedral units),<sup>65</sup> which can lead to stabilization of various intermediates including lower symmetry structures ( $C2/c$  and  $P\bar{1}$  as in the cases of  $\text{Na}_3\text{V}_2(\text{PO}_4)_3$  and  $\text{Na}_3\text{Nb}_2(\text{PO}_4)_3$ , respectively)<sup>59,63,66</sup> during cycling, leading to distinct electrochemical Li and Na intercalation pathways. Nevertheless, comprehensive

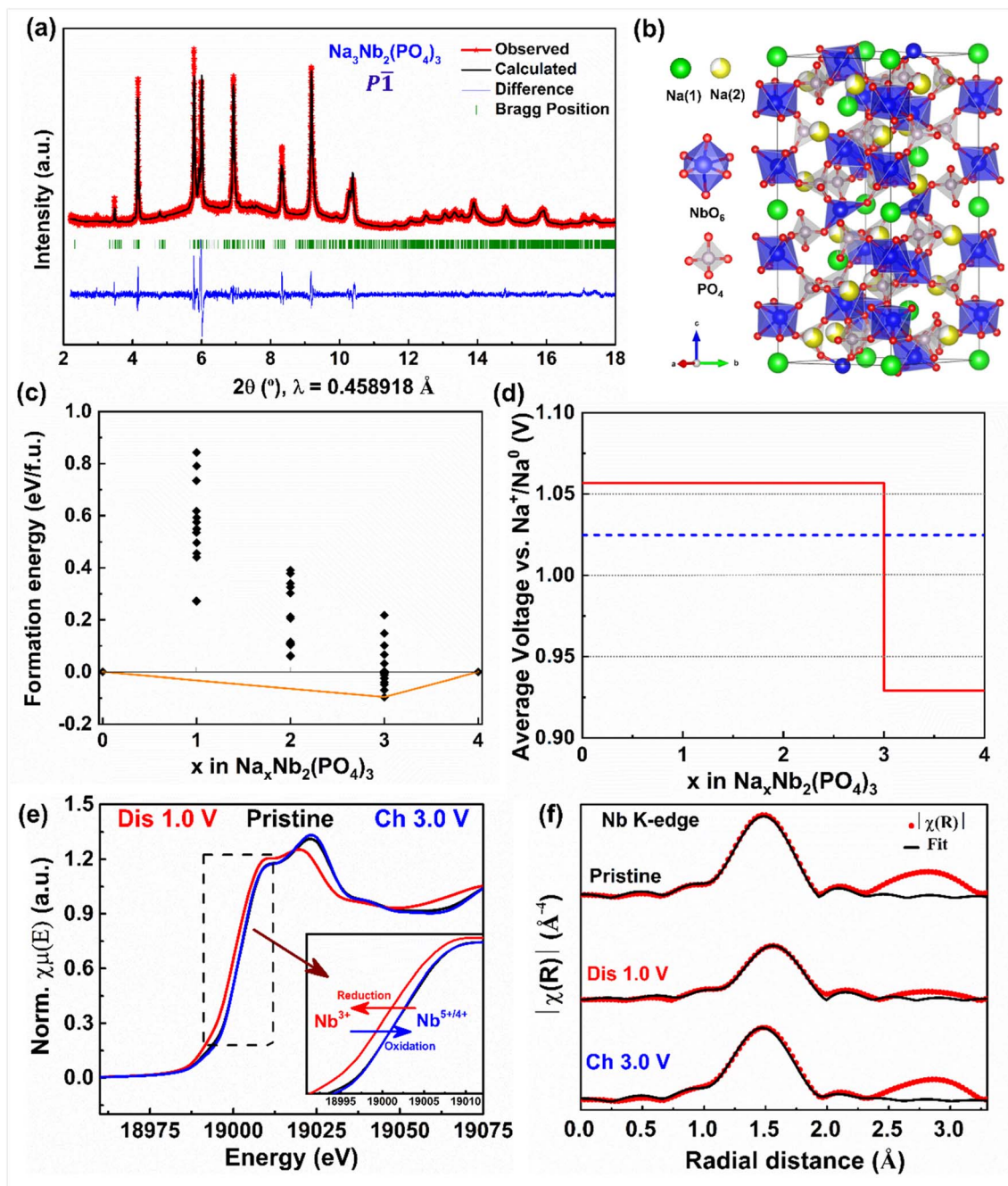


Fig. 4 (a) Le Bail refinement of synchrotron XRD and (b) crystal structure of  $\text{Na}_3\text{Nb}_2(\text{PO}_4)_3$ . (c) 0 K formation energy and (d) voltage plots (vs. Na) as a function of Na concentration ( $x$ ) in the  $\text{Na}_x\text{Nb}_2(\text{PO}_4)_3$  formula unit. The formation energy in (c) is referenced to the  $\text{Nb}_2(\text{PO}_4)_3$  (fully empty) and  $\text{Na}_4\text{Nb}_2(\text{PO}_4)_3$  (fully sodiated) compositions. The orange line in (c) indicates the convex hull, *i.e.*, the collection of lowest energy Na-vacancy configurations in  $\text{Na}_x\text{Nb}_2(\text{PO}_4)_3$ , while the black diamonds indicate metastable configurations. The dashed black line in (d) indicates the overall average voltage across the entire Na concentration in  $\text{Nb}_2(\text{PO}_4)_3$ . (e) XANES and (f) EXAFS plots of the NASICON- $\text{Nb}_2(\text{PO}_4)_3$  anode collected at the Nb K-edge.

studies involving short-range and long-range structural probes and DFT calculations are required to fully elucidate the structure–property relationship of the  $\text{Nb}_2(\text{PO}_4)_3$  anode.

Lastly, we have evaluated the rate performances and cycling stabilities of  $\text{Nb}_2(\text{PO}_4)_3/\text{Li}$  and  $\text{Nb}_2(\text{PO}_4)_3/\text{Na}$  cells at different C-rates. The  $\text{Nb}_2(\text{PO}_4)_3/\text{Li}$  cell delivers discharge capacities of 186, 174, 164, 155, and 142  $\text{mA h g}^{-1}$  at C/10, C/5, C/2, 1C, and 2C

rates, respectively, whereas the  $\text{Nb}_2(\text{PO}_4)_3/\text{Na}$  cell shows capacities of 172, 163, 153, 144 and 129  $\text{mA h g}^{-1}$  under similar experimental conditions (Fig. 5c). Upon cycling at C/10 rate, the  $\text{Nb}_2(\text{PO}_4)_3/\text{Li}$  and  $\text{Nb}_2(\text{PO}_4)_3/\text{Na}$  cells exhibit stable discharge capacities greater than 184 and 156  $\text{mA h g}^{-1}$ , respectively, for 20 cycles (Fig. 5d). Further, we assessed their cycling stability at 1C rate (Fig. 5e). The  $\text{Nb}_2(\text{PO}_4)_3/\text{Li}$  and  $\text{Nb}_2(\text{PO}_4)_3/\text{Na}$  cells exhibit



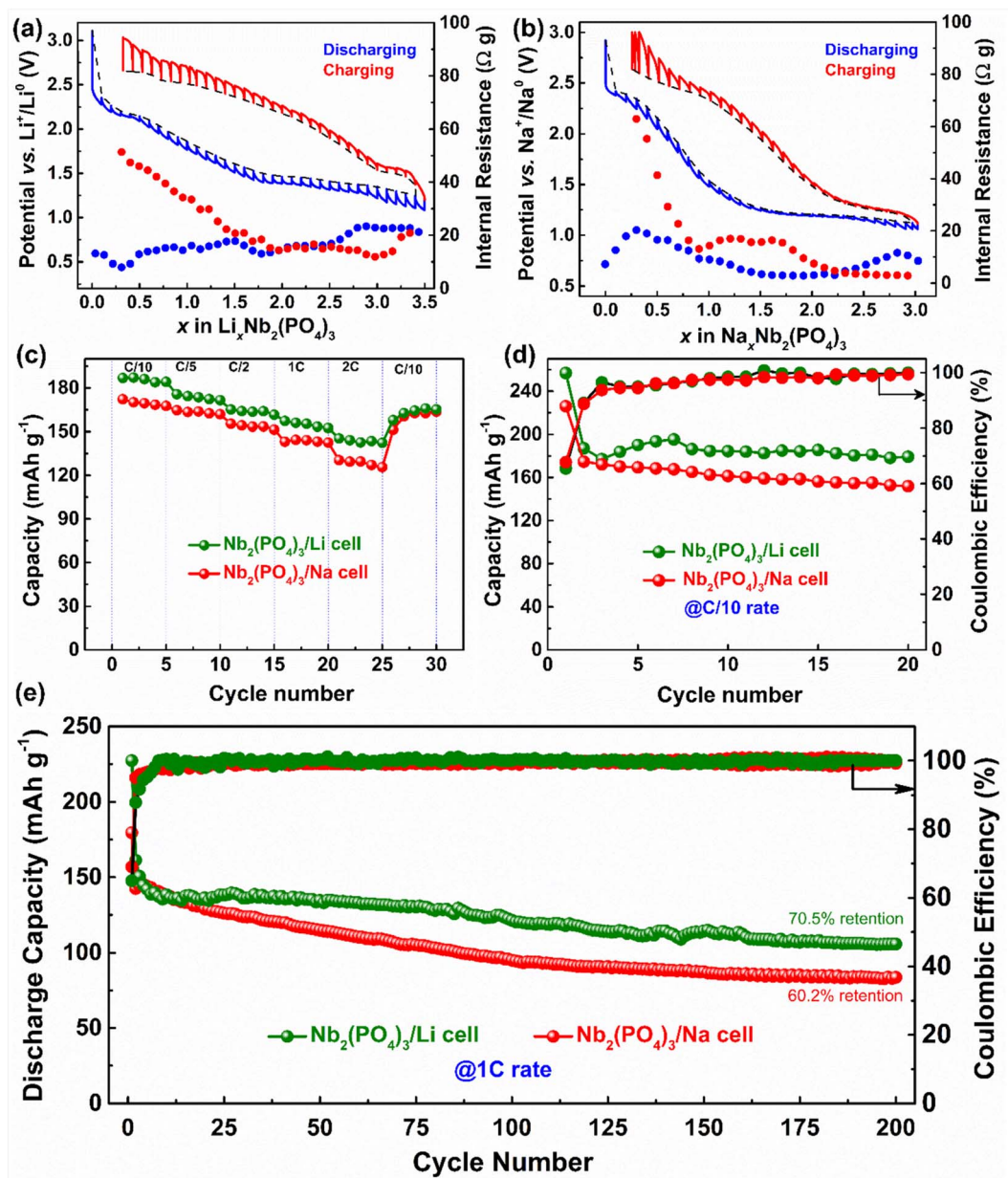


Fig. 5 GITT curves and calculated internal resistance for (a)  $\text{Nb}_2(\text{PO}_4)_3/\text{Li}$  and (b)  $\text{Nb}_2(\text{PO}_4)_3/\text{Na}$  cells. Rate capability (c), capacity retention at C/10 (d) and 1C (e) plots of  $\text{Nb}_2(\text{PO}_4)_3/\text{Li}$  and  $\text{Nb}_2(\text{PO}_4)_3/\text{Na}$  cells.

first/second cycle discharge capacities of 227/161 and 179/142  $\text{mA h g}^{-1}$ , respectively. The large discrepancies in discharge capacities between the first and second cycles can be attributed to the electrolyte decomposition and the entrapment of Li and Na ions in the NASICON framework. In the subsequent cycles, the discharge capacities of the  $\text{Nb}_2(\text{PO}_4)_3/\text{Li}$  cell slowly decrease and stabilize around 122  $\text{mA h g}^{-1}$  (after 100 cycles) and the cell still delivers a discharge capacity of 100  $\text{mA h g}^{-1}$  after 200 cycles. The  $\text{Nb}_2(\text{PO}_4)_3/\text{Na}$  cell retains 60.2% of its second discharge capacity after 200 cycles. The lower capacities obtained at high C-rate could be due to micron-size active particles in the as-prepared anode (Fig. S4<sup>†</sup>). It is also worth mentioning here that upon lowering the discharge voltage to 0.9 V, the capacity decay is faster in  $\text{Nb}_2(\text{PO}_4)_3/\text{Na}$  cells due to significant electrolyte

degradation (Fig. S5<sup>†</sup>). Further studies to improve the cycling performance of the  $\text{Nb}_2(\text{PO}_4)_3$  anode as well as to build full Li- and Na-ion cells are in progress. It is important to note that the integration of the NASICON- $\text{Nb}_2(\text{PO}_4)_3$  anode and the NASICON- $\text{Na}_3\text{V}_2(\text{PO}_4)_3$  cathode with a suitable electrolyte is expected to produce a higher energy density Na-ion battery compared to the Ti- and V-based anodes (Fig. S6<sup>†</sup>).<sup>67</sup>

## Conclusion

In conclusion, we have successfully synthesized polycrystalline  $\text{Nb}_2(\text{PO}_4)_3$  and demonstrated its potential application as an anode material for Li- and Na-ion batteries. The NASICON- $\text{Nb}_2(\text{PO}_4)_3$  reversibly exchanged Li and Na ions at average

voltages of 1.86 V and 1.46 V vs.  $\text{Li}^+/\text{Li}^0$  and  $\text{Na}^+/\text{Na}^0$  with intercalation capacities of  $\sim 167$  and  $150 \text{ mA h g}^{-1}$ , respectively. Our *in situ* XRD measurements revealed multiple-phase transformations during Li and Na intercalation with the formation of short-range ordered  $\text{Li}_3\text{Nb}_2(\text{PO}_4)_3$  and triclinic (*P1*)- $\text{Na}_3\text{Nb}_2(\text{PO}_4)_3$  at the end of discharge. Our DFT calculations predicted the  $\text{Na}_3\text{Nb}_2(\text{PO}_4)_3$  composition to be stable in the  $\text{Na-Nb}_2(\text{PO}_4)_3$  pseudo-binary system, in agreement with the *in situ* XRD results. The distinct electrochemical Li and Na intercalation behavior of the  $\text{Nb}_2(\text{PO}_4)_3$  anode can be ascribed to the relative differences in size, filling of crystallographic sites and chemical characters of Li and Na ions. Although the micron-sized anode showed moderate storage capacities ( $\sim 106$  and  $84 \text{ mA h g}^{-1}$  for Li and Na cells, respectively) at higher C-rate (1C) after 200 cycles, further optimization of the electrode and electrolytes is expected to produce better performance, which can aid in building high energy density Na-ion batteries.

## Conflicts of interest

The authors declare no conflict of interest.

## Author contributions

All authors have approved the final version of the manuscript.

## Acknowledgements

This work was supported by the Department of Science & Technology (DST), Government of India (DST/TMD/MES/2K18/188). B. P. thanks CSIR for the research fellowship. G. S. G. acknowledges support from the Science and Engineering Research Board (SERB), Government of India, under sanction number IPA/2021/000007. D. D. acknowledges financial assistance from Ministry of Human Resource Development, Government of India. The authors acknowledge DESY (Hamburg, Germany), a member of the Helmholtz Association HGF, for the provision of experimental facilities. Parts of this research were carried out at PETRA III and the authors thank Dr Edmund Welter for his assistance in using Beamline P65 to perform X-ray absorption spectroscopy measurements and DST for financial assistance for the measurement at DESY. Synchrotron X-ray diffraction data were collected at 11-BM (mail-in program; GUP-77942), at the Advanced Photon Source, Argonne National Laboratory, a U.S. Department of Energy (DOE) Office of Science User Facility operated for the DOE Office of Science by Argonne National Laboratory under Contract No. DE-AC02-06CH11357. A portion of the density functional theory calculations showcased in this work were performed with the computational resources provided by the Supercomputer Education and Research Center, Indian Institute of Science.

## References

- Z. Yang, J. Zhang, M. C. W. Kintner-Meyer, X. Lu, D. Choi, J. P. Lemmon and J. Liu, *Chem. Rev.*, 2011, **111**, 3577–3613.
- B. Dunn, H. Kamath and J. M. Tarascon, *Science*, 2011, **334**, 928–935.
- T. Kim, W. Song, D. Y. Son, L. K. Ono and Y. Qi, *J. Mater. Chem. A*, 2019, **7**, 2942–2964.
- Y. Tian, G. Zeng, A. Rutt, T. Shi, H. Kim, J. Wang, J. Koettgen, Y. Sun, B. Ouyang, T. Chen, Z. Lun, Z. Rong, K. Persson and G. Ceder, *Chem. Rev.*, 2021, **121**, 1623–1669.
- N. Tapia-Ruiz, A. R. Armstrong, H. Alptekin, M. A. Amores, H. Au, J. Barker, R. Boston, W. R. Brant, J. M. Brittain, Y. Chen, M. Chhowalla, Y. S. Choi, S. I. R. Costa, M. C. Ribadeneyra, S. A. Cussen, E. J. Cussen, W. I. F. David, A. V. Desai, S. A. M. Dickson, E. I. Ewaka, J. D. Forero-Saboya, C. P. Grey, J. M. Griffin, P. Gross, X. Hua, J. T. S. Irvine, P. Johansson, M. O. Jones, M. Karlsmo, E. Kendrick, E. Kim, O. V. Kolosov, Z. Li, S. F. L. Mertens, R. Mogensen, L. Monconduit, R. E. Morris, A. J. Naylor, S. Nikman, C. A. O'Keefe, D. M. C. Ould, R. G. Palgrave, P. Poizot, A. Ponrouch, S. Renault, E. M. Reynolds, A. Rudola, R. Sayers, D. O. Scanlon, S. Sen, V. R. Seymour, B. Silván, M. T. Sougrati, L. Stievano, G. S. Stone, C. I. Thomas, M. M. Titirici, J. Tong, T. J. Wood, D. S. Wright and R. Younesi, *J. Phys. Energy*, 2021, 3031503.
- K. Chayambuka, G. Mulder, D. L. Danilov and P. H. L. Notten, *Adv. Energy Mater.*, 2020, **10**, 2001310.
- E. Goikolea, V. Palomares, S. Wang, I. R. de Larramendi, X. Guo, G. Wang and T. Rojo, *Adv. Energy Mater.*, 2020, **10**, 2002055.
- J. M. Tarascon, *Joule*, 2020, **4**, 1616–1620.
- E. Irisarri, A. Ponrouch and M. R. Palacin, *J. Electrochem. Soc.*, 2015, **162**, A2476–A2482.
- G. N. Zhu, Y. G. Wang and Y. Y. Xia, *Energy Environ. Sci.*, 2012, **5**, 6652–6667.
- K. M. Colbow, J. R. Dahn and R. R. Haering, *J. Power Sources*, 1989, **26**, 397–402.
- J. F. Colin, V. Pralong, M. Hervieu, V. Caignaert and B. Raveau, *Chem. Mater.*, 2008, **20**, 1534–1540.
- B. Guo, X. Yu, X. G. Sun, M. Chi, Z. A. Qiao, J. Liu, Y. S. Hu, X. Q. Yang, J. B. Goodenough and S. Dai, *Energy Environ. Sci.*, 2014, **7**, 2220–2226.
- S. Qian, H. Yu, L. Yan, H. Zhu, X. Cheng, Y. Xie, N. Long, M. Shui and J. Shu, *ACS Appl. Mater. Interfaces*, 2017, **9**, 30608–30616.
- Q. Cheng, J. Liang, Y. Zhu, L. Si, C. Guo and Y. Qian, *J. Mater. Chem. A*, 2014, **2**, 17258–17262.
- P. Senguttuvan, G. Rousse, V. Seznec, J. M. Tarascon and M. R. Palacin, *Chem. Mater.*, 2011, **23**, 4109–4111.
- W. Wang, Y. Liu, X. Wu, J. Wang, L. Fu, Y. Zhu, Y. Wu and X. Liu, *Adv. Mater. Technol.*, 2018, **3**, 1800004.
- Y. Sun, L. Zhao, H. Pan, X. Lu, L. Gu, Y. S. Hu, H. Li, M. Armand, Y. Ikuhara, L. Chen and X. Huang, *Nat. Commun.*, 2013, **4**, 1870.
- H. Gao and J. B. Goodenough, *Angew. Chem., Int. Ed.*, 2016, **55**, 12768–12772.
- J. Wang, Y. Wang, D. H. Seo, T. Shi, S. Chen, Y. Tian, H. Kim and G. Ceder, *Adv. Energy Mater.*, 2020, **10**, 1–10.

- 21 S. Ghosh, N. Barman, M. Mazumder, S. K. Pati, G. Rousse and P. Senguttuvan, *Adv. Energy Mater.*, 2020, **10**, 1902918.
- 22 S. Chen, C. Wu, L. Shen, C. Zhu, Y. Huang, K. Xi, J. Maier and Y. Yu, *Adv. Mater.*, 2017, **29**, 1700431.
- 23 Z. Jian, Y. S. Hu, X. Ji and W. Chen, *Adv. Mater.*, 2017, **29**, 1601925.
- 24 M. Guin and F. Tietz, *J. Power Sources*, 2015, **273**, 1056–1064.
- 25 Z. Zhang, Z. Zou, K. Kaup, R. Xiao, S. Shi, M. Avdeev, Y. S. Hu, D. Wang, B. He, H. Li, X. Huang, L. F. Nazar and L. Chen, *Adv. Energy Mater.*, 2019, **9**, 1–14.
- 26 Z. Deng, G. Sai Gautam, S. K. Kolli, J. N. Chotard, A. K. Cheetham, C. Masquelier and P. Canepa, *Chem. Mater.*, 2020, **32**, 7908–7920.
- 27 R. Kahlaoui, K. Arbi, I. Sobrados, R. Jimenez, J. Sanz and R. Ternane, *Inorg. Chem.*, 2017, **56**, 1216–1224.
- 28 C. Masquelier, C. Wurm, J. Rodríguez-Carvajal, J. Gaubicher and L. Nazar, *Chem. Mater.*, 2000, **12**, 525–532.
- 29 A. Aatiq, M. Ménétrier, L. Croguennec, E. Suard and C. Delmas, *J. Mater. Chem.*, 2002, **12**, 2971–2978.
- 30 C. Delmas, F. Cherkaoui, A. Nadiri and P. Hagenmuller, *Mater. Res. Bull.*, 1987, **22**, 631–639.
- 31 S. Patoux and C. Masquelier, *Chem. Mater.*, 2002, **14**, 5057–5068.
- 32 M. Wu, W. Ni, J. Hu and J. Ma, *Nano-Micro Lett.*, 2019, **11**, 1–36.
- 33 P. Senguttuvan, G. Rousse, M. E. Arroyo Y De Dompablo, H. Vezin, J. M. Tarascon and M. R. Palacín, *J. Am. Chem. Soc.*, 2013, **135**, 3897–3903.
- 34 Z. Jian, L. Zhao, H. Pan, Y. S. Hu, H. Li, W. Chen and L. Chen, *Electrochem. Commun.*, 2012, **14**, 86–89.
- 35 Z. Jian, W. Han, X. Lu, H. Yang, Y.-S. Hu, J. Zhou, Z. Zhou, J. Li, W. Chen, D. Chen, L. Chen, Z. L. Jian, W. Z. Han, X. Lu, H. X. Yang, Y. Hu, J. Q. Li, L. Q. Chen, J. Zhou, W. Chen, D. F. Chen and Z. B. Zhou, *Adv. Energy Mater.*, 2013, **3**, 156–160.
- 36 O. Tillement, J. C. Couturier, J. Angenault and M. Quarton, *Solid State Ionics*, 1991, **48**, 249–255.
- 37 J. Liu, K. Lin, Y. Zhao, Y. Zhou, X. Hou, X. Liu, H. Lou, K. H. Lam and F. Chen, *J. Mater. Chem. A*, 2021, **9**, 10437–10446.
- 38 S. Ghosh, N. Jose, B. Senthilkumar, P. Amonpattaratkit and P. Senguttuvan, *J. Electrochem. Soc.*, 2021, 168050534.
- 39 T. Zhu, P. Hu, X. Wang, Z. Liu, W. Luo, K. A. Owusu, W. Cao, C. Shi, J. Li, L. Zhou and L. Mai, *Adv. Energy Mater.*, 2019, **9**, 2–7.
- 40 I. V. Zatovsky, *Acta Crystallogr., Sect. E: Struct. Rep. Online*, 2010, **66**, i12.
- 41 B. Ouyang, J. Wang, T. He, C. J. Bartel, H. Huo, Y. Wang, V. Lacivita, H. Kim and G. Ceder, *Nat. Commun.*, 2021, **12**, 1–11.
- 42 A. Leclaire, M.-M. Borel, A. Grandin and B. Raveau, *Acta Crystallogr., Sect. C: Cryst. Struct. Commun.*, 1989, **45**, 699–701.
- 43 J. Rodríguez-Carvajal, *Phys. B Condens. Matter*, 1993, **192**, 55–69.
- 44 M. Newville, *J. Synchrotron Radiat.*, 2001, **8**, 322–324.
- 45 B. Ravel and M. Newville, *J. Synchrotron Radiat.*, 2005, **12**, 537–541.
- 46 G. Kresse and J. Hafner, *Phys. Rev. B: Condens. Matter Mater. Phys.*, 1993, **47**, 558.
- 47 G. Kresse and J. Furthmüller, *Phys. Rev. B: Condens. Matter Mater. Phys.*, 1996, **54**, 11169.
- 48 G. Kresse and D. Joubert, *Phys. Rev. B: Condens. Matter Mater. Phys.*, 1999, **59**, 1758.
- 49 J. Sun, A. Ruzsinszky and J. Perdew, *Phys. Rev. Lett.*, 2015, 115036402.
- 50 M. Hellenbrandt, *Crystallogr. Rev.*, 2004, **10**, 17–22.
- 51 S. P. Ong, W. D. Richards, A. Jain, G. Hautier, M. Kocher, S. Cholia, D. Gunter, V. L. Chevrier, K. A. Persson and G. Ceder, *Comput. Mater. Sci.*, 2013, **68**, 314–319.
- 52 B. Singh, Z. Wang, S. Park, G. S. Gautam, J. N. Chotard, L. Croguennec, D. Carlier, A. K. Cheetham, C. Masquelier and P. Canepa, *J. Mater. Chem. A*, 2021, **9**, 281–292.
- 53 Z. Wang, S. Park, Z. Deng, D. Carlier, J. N. Chotard, L. Croguennec, G. S. Gautam, A. K. Cheetham, C. Masquelier and P. Canepa, *J. Mater. Chem. A*, 2022, **10**, 209–217.
- 54 M. Bianchini, F. Fauth, N. Brisset, F. Weill, E. Suard, C. Masquelier and L. Croguennec, *Chem. Mater.*, 2015, **27**, 3009–3020.
- 55 M. Bianchini, J. M. Ateba-Mba, P. Dagault, E. Bogdan, D. Carlier, E. Suard, C. Masquelier and L. Croguennec, *J. Mater. Chem. A*, 2014, **2**, 10182–10192.
- 56 M. Galceran, J. Rikarte, M. Zarrabeitia, M. C. Pujol, M. Aguiló and M. Casas-Cabanas, *ACS Appl. Energy Mater.*, 2019, **2**, 1923–1931.
- 57 P. Senguttuvan, G. Rousse, H. Vezin, J. M. Tarascon and M. R. Palacín, *Chem. Mater.*, 2013, **25**, 2391–2393.
- 58 H. Kabbour, D. Coillot, M. Colmont, C. Masquelier and O. Mentré, *J. Am. Chem. Soc.*, 2011, **133**, 11900–11903.
- 59 P. Senguttuvan, G. Rousse, M. E. Arroyo Y De Dompablo, H. Vezin, J. M. Tarascon and M. R. Palacín, *J. Am. Chem. Soc.*, 2013, **135**, 3897–3903.
- 60 Z. Deng, T. P. Mishra, E. Mahayoni, Q. Ma, A. J. K. Tieu, O. Guillon, J. N. Chotard, V. Seznec, A. K. Cheetham, C. Masquelier, G. S. Gautam and P. Canepa, *Nat. Commun.*, 2022, **13**, 1–14.
- 61 G. Yan, S. Mariyappan, G. Rousse, Q. Jacquet, M. Deschamps, R. David, B. Mirvaux, J. W. Freeland and J. M. Tarascon, *Nat. Commun.*, 2019, **10**, 585.
- 62 J. Kim, W. Lee, J. Seok, E. Lee, W. Choi, H. Park, S. Yun, M. Kim, J. Lim and W. S. Yoon, *J. Energy Chem.*, 2022, **66**, 226–236.
- 63 C. Masquelier, C. Wurm, J. Rodríguez-Carvajal, J. Gaubicher and L. Nazar, *Chem. Mater.*, 2000, **12**, 525–532.
- 64 Z. Zhang, Z. Zou, K. Kaup, R. Xiao, S. Shi, M. Avdeev, Y. S. Hu, D. Wang, B. He, H. Li, X. Huang, L. F. Nazar and L. Chen, *Adv. Energy Mater.*, 2019, **9**, 1902373.
- 65 S. Zhou, G. Barim, B. J. Morgan, B. C. Melot and R. L. Brutchey, *Chem. Mater.*, 2016, **28**, 4492–4500.
- 66 J. N. Chotard, G. Rousse, R. David, O. Mentré, M. Courty and C. Masquelier, *Chem. Mater.*, 2015, **27**, 5982–5987.
- 67 M. K. Sadan, A. K. Haridas, H. Kim, C. Kim, G. B. Cho, K. K. Cho, J. H. Ahn and H. J. Ahn, *Nanoscale Adv.*, 2020, **2**, 5166–5170.